



On the subsonic near-wake of a space launcher configuration with exhaust jet

Experimental investigation by means of particle image velocimetry (PIV) on the subsonic (Mach 0.5–0.9) near-wake flow of a space launcher configuration with a cold, over-expanded, supersonic jet

Dominik Saile¹ · Viktor Kühl¹ · Ali Gülhan¹

Received: 15 February 2019 / Revised: 26 July 2019 / Accepted: 27 August 2019
© The Author(s) 2019

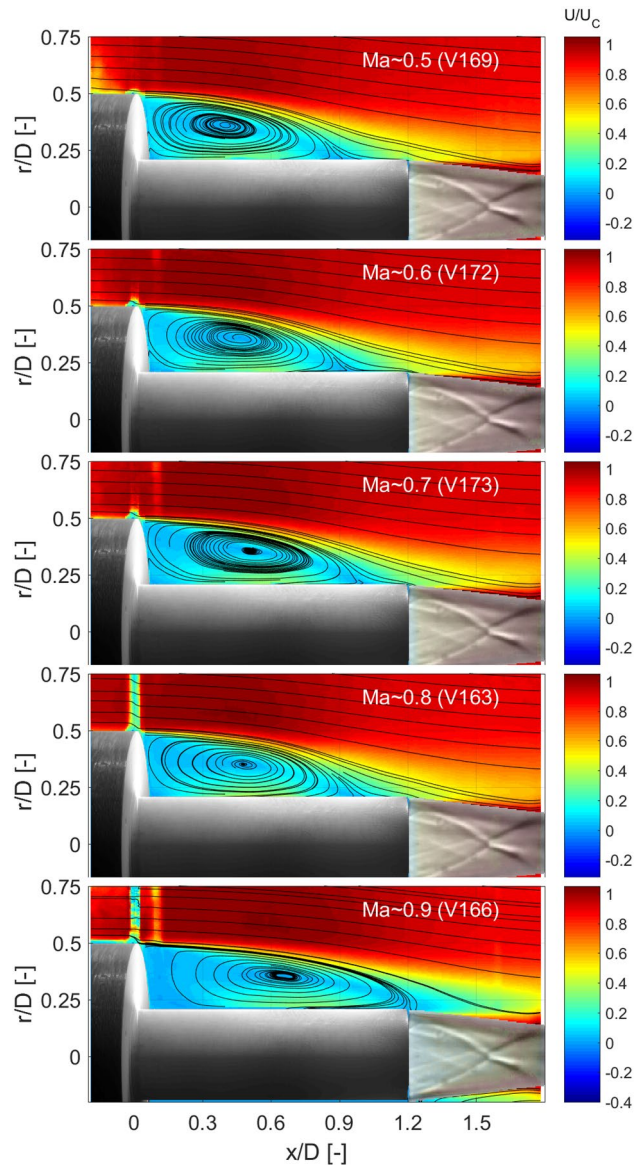
Abstract

The Ariane 5 failure flight 157 made clear that the loads in the base region of space launcher configurations were underestimated and its near-wake dynamics required more attention. In the recent years, many studies have been published on buffet/buffeting in the critical high subsonic flow regime. Nevertheless, not much experimental data are available on the interaction of the ambient flow with an exhaust jet over a wide subsonic Mach number range. Further, a preceding study without exhaust jet revealed questions regarding a similar distribution of the velocity and Reynolds stress in the near-wake if scaled with the reattachment length. Consequently, a generic space launcher configuration featuring a cold, supersonic, over-expanded jet is investigated experimentally in the vertical test section Cologne (VMK) by means of particle image velocimetry (PIV) for five subsonic Mach numbers ranging from 0.5 to 0.9 with corresponding Reynolds numbers between $Re_D = 0.8 \times 10^6$ to 1.6×10^6 . The velocity and Reynolds stress distribution are provided for the near-wake flow and additionally for the incoming boundary layer. Just as in the preceding study, self-similar features are found in the flow field as long as the separated shear layer reattaches on the solid nozzle wall. Substantial changes are then measured for an alternating (hybrid) reattachment between the solid nozzle wall and supersonic exhaust jet as found for Mach 0.8, one of them being the increased axial turbulence in the recirculation bubble due to a ‘dancing’ large-scale, clockwise-rotating vortex.

✉ Dominik Saile
dominik.saile@dlr.de

¹ Institute of Aerodynamics and Flow Technology, Supersonic and Hypersonic Technology Department, DLR German Aerospace Center, Linder Höhe, 51147 Cologne, Germany

Graphic abstract



1 Introduction

The inquiry board in charge of the investigation of space transportation system Ariane 5 flight 157 in 2002 came to the conclusion that one of the most probable reasons for the failure was a ‘non-exhaustive definition of the loads to which the Vulcain 2 engine is subjected during flight’. This incident was the driver for a number of base flow investigations with the objective of understanding and quantifying these loads. In the early phase of the ascent, Ariane 5 is mostly exposed to mechanical loads of which the buffeting loads occurring

in the transonic flow regime and predominantly at Mach 0.8 are seen as most critical (David and Radulovic 2005; Schwane 2015).

During its ascent through the atmosphere, the air flow passing the Ariane 5 separates at the base and deflects toward the symmetry axis where it impinges—depending on the conditions—either on the solid nozzle or the jet. The wake flow is generally highly dynamic and so is the impingement or reattachment process of the shear layer, which in turn leads to wall pressure fluctuations and consequently to the excitation of structural nozzle oscillations. The interaction

between the exciting aerodynamic forces in the near-wake (buffet) and structural response is then called buffeting. The dynamics of buffet/buffeting and the governing mechanisms have been the main objective of past studies.

There are studies that specifically address issues of the Ariane 5 configuration. In other words, these studies take as foundation an exact representation of its (base) geometry (e.g., Wong et al. 2007; Schrijer et al. 2011; Hannemann et al. 2011; Pain et al. 2014; Schwane 2015; Lüdeke et al. 2015; Weiss and Deck 2018). But when it comes to the governing mechanisms, most studies use a generic representation to simplify the interpretation and generalize the findings. Among others, significant contribution in that respect for the subsonic and transonic flow regime came from Fuchs et al. (1979), Deprés et al. (2004), Deck and Thorigny (2007), Weiss et al. (2009), Weiss and Deck (2013), Schrijer et al. (2014), Scharnowski (2013), Scharnowski et al. (2015, 2016), Statnikov et al. (2016, 2017) and van Gent et al. (2017a, b).

On the search, mode decomposition methods have proven to be a valuable tool and aspects to the current status of the findings accumulated over the years with additional new insights as presented in the work by Statnikov et al. (2017). In that study, a reduced order analysis, or to be more specific, a dynamic mode decomposition (DMD) was applied on the numerical simulation (zonal RANS-LES) results. The authors reported a longitudinal *cross-pumping* motion of the separation bubble in the stream-wise direction oscillating with a non-dimensional frequency of $Sr_D \approx 0.1$. Here, 'cross' denotes the repeating pattern in the circumferential direction. Interrelated or coupled with *cross-pumping* is a motion identified as *cross-flapping* of the shear layer. It is considered as coupled, since a vortical structure is shed from the main vortex every time the separation bubble is close to the nozzle exit, which happens twice per longitudinal *cross-pumping* cycle, ergo with a frequency of $Sr_D \approx 0.2$. Due to its pronounced antisymmetry, this mode is considered as the predominant mechanism for side loads. The third mode found in the wake flow is a higher harmonic of the main vortex shedding mode taking place with a frequency $Sr_D \approx 0.35$. It is characterized as *swinging* motion of the shear layer. Finally, Statnikov et al. (2017) rule out the hypothesis of other works that the *cross-flapping* mode is of helical nature. Instead, the orientation of the vortices in a momentarily longitudinal plane changes arbitrarily over time.

Of the above listed studies, only the study of Deprés et al. (2004), Weiss and Deck (2013) and van Gent et al. (2017a, b) are experimental or contain experimental parts on an axisymmetric configuration with an exhaust jet. In other words, there is a lack of experimental data simulating a space launcher with exhaust jet. The current study has the objective to contribute insights into the velocity field

and Reynolds stress distribution over a wide subsonic range from Mach 0.5 to 0.9. The work is an extension of a preceding investigation on the exact same configuration without exhaust jet (Saile et al. 2019). That study found a similar velocity and Reynolds stress distribution for the investigated flow range independently of the Mach and Reynolds number if scaled with the shear layer reattachment length. This finding serves as further research question, and thus, the similarity of the corresponding distributions will be scrutinized for the configuration with jet.

To address the research questions, wind tunnel experiments are conducted in the vertical test section Cologne (VMK) in the subsonic/transonic flow regime on a generic space launcher configuration with exhaust jet. Data are captured by means of particle image velocimetry (PIV) and analyzed with respect to the velocity and the Reynolds stress distribution. Additionally, the incoming boundary layers at various Mach numbers are characterized with respect to mean and fluctuating properties to provide further information of the upstream conditions and to assess its impact on the wake flow. The results are compared with literature.

The overarching driver for the study at hand is to support the community with data for the definition of the loads on the base of space launcher geometries. In short, the objective is to contribute to the development of improved design guidelines for space launchers to prevent incidents as the Ariane 5 failure flight 157.

Therefore, the current results must obviously feature a relation to the Ariane 5 flight. Thus, some commonalities and deviations are presented in the following to provide a 'feel' for the similarity to the real flight. The current investigations simulate the flight of Ariane 5 at an altitude between 1.6 and 5.4 km. There, the Ariane 5 nozzle flow is still over-expanded. It also might be interesting to mention that the trajectory simulations predict adapted nozzle flow conditions at an altitude of about 14 km at Mach 1.8.

The pressure ratio between the nozzle exit flow and the ambient flow determines if the nozzle flow is over- or under-expanded. In both cases, meaning in flight and simulation, it is such that the nozzle flow is over-expanded. In detail, the pressure ratio between the ambient and the nozzle exit pressure for Ariane 5 is at about 0.25 at Mach 0.8, while it is at 0.36 for the corresponding experimental setup. This is actually relatively comparable, meaning the plume shape is also relatively similar. Further adjustments to decrease that factor are not possible with the current configuration due to the risk of condensation in the cold nozzle flow.

The cold nozzle flow is a notable deviation to the real flight condition. The exit flow velocity is about six to seven times larger for the Vulcain 2 engine. As a result, it is to be expected that, in the real flight, the base suction effect (Schoones and Bannink 1998; Deprés et al. 2004; Wolf 2013) is stronger due to the higher velocity in the shear

layer of the jet. This effect in turn leads to a smaller base pressure level and a reduced recirculation bubble length. Furthermore, the conical nozzle used here—instead of the thrust-optimised contour (TOC) nozzle as for Vulcain 2—is justified since the investigation of a generic configuration is of interest. TOC nozzles instead feature complex shock patterns inside of the nozzle, which complicate general deductions. However, it shall be mentioned that the larger deflection angle of the conical nozzle also influences the base flow: it causes an increase of the base pressure (Wong et al. 2007).

The near-wake is obviously not only influenced by the effects associated with the conditions imposed by the nozzle flow, but also by the incoming flow upstream from the flow separation at the base. Roshko and Lau (1965) found flow similarity features of the recirculation bubble, which persist as long as the boundary layer can be considered as ‘thin’ (Westphal et al. 1984). In other words, the question is now as following: How does the incoming boundary layer of the experiments relate to the flight? For the predecessor investigations of the same configuration without jet (Saile et al. 2019), the ratio between the incoming turbulent boundary layer to the diameter of base is about 0.07 at, e.g., Mach 0.8. This is of the same order of what was approximated for Ariane 5. For the real flight, a ratio of 0.09 was calculated. The corresponding boundary layer thickness was determined by assuming a compressible turbulent boundary layer developing along a flat plate (Devenport and Schetz 2019) for the conditions at Mach 0.8.

The study is structured as following: Sect. 2 elaborates the test environment, measurement and analysis methods. Section 3 describes the measurement results, which are then discussed in Sect. 4. A conclusion and summary of the findings are provided at the end in Sect. 5.

2 Methods

The experiments were executed in the vertical test section Cologne (VMK). VMK is a blow-down type of wind tunnel featuring a vertical free test section for tests in the subsonic to supersonic range starting from Mach 0.5 up to 3.2 (Saile et al. 2015). The current experiments were conducted with a subsonic nozzle featuring an exit diameter of 340 mm.

The wind tunnel model integrated in the subsonic wind tunnel nozzle is shown as a sketch in Fig. 1. This upstream support is advantageous since there is no inherent displacement of the wind tunnel model, which could cause issues due to a blockage or choking effect of the flow (Goethert 1961). In fact, Weiss and Deck (2013) provided a detailed comparison between a free flight and wind tunnel flow for essentially the same base configuration. The most dominant influence was found in the fluctuations, which are influenced by the merging shear layers from the wind tunnel nozzle and

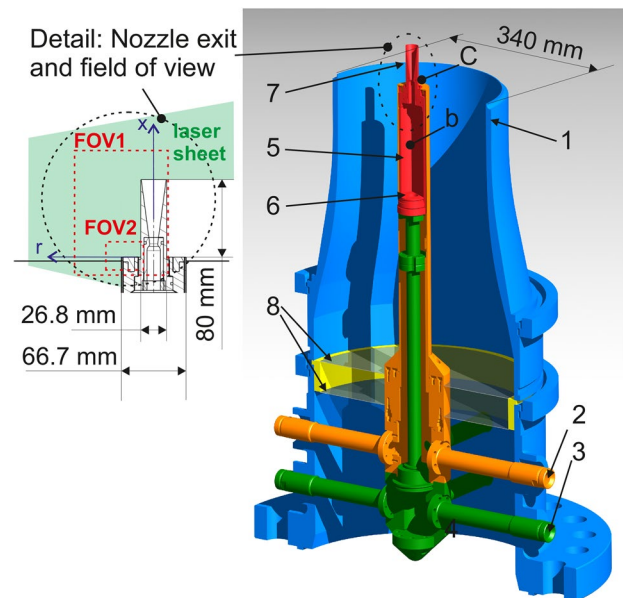


Fig. 1 Sketch of the wind tunnel model with the wind tunnel nozzle (blue), cold jet supply system (green) and the chamber (red). The graph further contains the field of views, which are used for the base and boundary layer flow investigations. They are denoted as *FOV1* and *FOV2*, respectively

wind tunnel model. However, in the predecessor study of the current series (Saile et al. 2019), this effect appeared negligible for the current experimental setup. This was attributed to the comparably large diameter ratio between the wind tunnel nozzle and the base of the model.

Upstream of the wind tunnel nozzle exit (Fig. 1), the wind tunnel nozzle (1) is equipped with support arms (2) and (3), which have three tasks. First, they keep the wind tunnel model in place; second, one or several supports can be used as access point for the harnessing of the sensors, and third, one support is used for the air supply. The support arms converge in a central mounting (4) on top of which is the combustion or reservoir chamber (5). The injector (6) and the nozzle (7) are exchangeable to realize various injection conditions and nozzle exit conditions, respectively. The wind tunnel nozzle is equipped with two levels of straighteners (8) downstream of the support arms to reduce perturbations.

Further details to the wind tunnel model are given in Fig. 2. The main component of this base representation of a space launcher configuration is a cylindrical main body with a cylindrical nozzle attached to its base. The first has a diameter of $D = 66.7$ mm and the second $d = 26.8$ mm. The smaller cylinder features a length of $L = 80$ mm. The geometry mimics the main generic components of the Ariane 5 base with respect to its scaling ($d/D \sim 0.4$, $L/D \sim 1.2$). Further, the base plate is 10.4 mm downstream from the wind tunnel nozzle exit. The nozzle has a conical contour and to avoid the occurrence of condensed oxygen in the cold

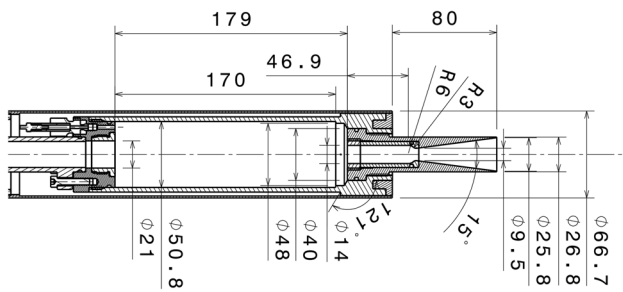


Fig. 2 Technical drawing focusing on the chamber and nozzle geometry. Units are given in millimeter

Table 1 Flow conditions for the various experiments

Run ID	VMK			Model	
	Ma_C (-)	U_C (ms ⁻¹)	Re_D (-)	$p_{0,b}$ (MPa)	$T_{0,b}$ (K)
V169	0.49	160.7	0.8×10^6	3.24	283.9
V172	0.59	193.0	1.0×10^6	3.25	286.6
V173	0.69	224.3	1.2×10^6	3.26	284.8
V163	0.79	257.5	1.4×10^6	3.31	283.8
V166	0.89	284.4	1.6×10^6	3.28	286.1

exhaust jet, it was chosen to limit the expansion ratio to $\epsilon = 7.37$, which is equivalent to a nozzle exit Mach number of 3.59 for an isentropic expansion of air.

The inflow conditions for each run are listed in Tables 1 and 2. The first table shows data for the near-wake flow analysis, and the second for the boundary layer considerations. In detail, they contain data for the ambient flow like the exit Mach number Ma_C , exit velocity U_C , exit Reynolds number Re_D based on the diameter of the main cylinder. Additionally, the chamber pressure $p_{0,b}$ and temperature $T_{0,b}$ of the wind tunnel model are listed. The exit Mach number was calculated under the assumption of an isentropic expansion by means of the reservoir and ambient pressure; the velocity is directly taken from the PIV results. The boundary layer velocity profiles, and thus the mean ambient flow velocities listed in Table 2, are extracted at a location directly downstream of the wind tunnel nozzle exit at $x/D = -0.02$. Due to corrupted results just upstream of the base for the investigation of the wake flow with field of view 1 (FOV1), the ambient flow velocity listed in Table 1 had to be determined farther downstream from the base. The ambient flow velocity is averaged over an area between $0.15 < x/D < 0.2$ and $0.7 < r/D < 0.8$. Note that the referred FOVs are specified below.

A classical 2D-2C PIV measurement setup was applied here which is practically equivalent to the setup described in Saile et al. (2019). An *Ultra CFR Nd:YAG* laser system of *Big Sky Laser* was used. Each laser pulse has an energy of

190 mJ at a wavelength of 532 nm. The sheet thickness was in the range of 0.5 mm. Perpendicular to the laser sheet, a *PCO1600* camera system by *PCO AG* was set up at a distance of about 200 mm for the acquisition of the particle images. The *LabSmith* timing unit by *LC880* controls the trigger pulses for both components with an accuracy of 100 ps. Dependent on the focus of the experiments, the camera was equipped with either of two different lenses by *Carl Zeiss AG* to resolve two different FOVs. The *Makro-Planar 2/35 ZF* was used for a global view of the wake featuring a FOV (named *FOV1*) of $134 \times 100 \text{ mm}^2$. The aperture number was set to 16. Due to the high depth of focus, the choice for the aperture setting has turned out to be unfortunate. The wind tunnel nozzle is faintly visible in the background of the *FOV1* raw images for occasionally weak seeding. For this reason, results of *FOV1* are not discussed in that flawed range, which is marked in the corresponding figures as *excl.* for excluded. The flawed range is located upstream from $x/D < 0.15$ and related to the incoming free stream, meaning $r/D > 0.5$. The *Makro-Planar 2/100 ZF* was applied for boundary layer measurements with an aperture number setting of 11. The lens provided a FOV of $24 \times 31 \text{ mm}^2$, which is equivalent to a spatial resolution increase factor of about 4.3. The latter is named *FOV2*. Both FOVs are depicted in Fig. 1, which also shows the coordinate system originating in the symmetry axis on the base. Seeding was accomplished with an in-house developed seeding generator providing titanium dioxide particles. Titanium dioxide of the type *K1002* from *Kronos International, Inc.* is used as seeding material. The particles are injected into the flow at position ‘A’ (Fig. 1). The jet is not seeded.

The analysis of the images was executed with *PIVview V3.60* by *PIVTEC GmbH*. The selection of the setting of image sampling was based on the experience and results of the preceding study without jet (Saile et al. 2019). In total, a number of 345 images per run were evaluated with a window size of $32 \times 16 \text{ px}$ with an overlap of $4 \times 4 \text{ px}$. In physical units, one interrogation window without overlap has a size of $2.68 \times 1.34 \text{ mm}^2$ in case of *FOV1* (Run ID: V169, V172, V173, V163, V166) and $0.62 \times 0.31 \text{ mm}^2$ for *FOV2* (Run ID: V212, V208, V210, V211). Non-dimensionalized with the diameter of the main body, this corresponds to 0.04×0.02 and 0.0093×0.0046 , respectively. For both FOVs, the multi-grid interrogation method with grid refinement was applied, the *Whittaker* reconstruction (Raffel et al. 2007) was used for the sub-pixel peak fit, and on the final pass, a B-spline interpolation scheme of third order was applied to cover the aspect of adaptive image deformation. The data were not interpolated.

Further, the raw images for boundary layer measurements (*FOV2*) were shifted to level out the movement of the wind tunnel model. The standard deviation of the lateral movement between the camera and the wind tunnel model was

found to be $\leq 40 \mu\text{m}$. For field of view *FOV1*, the relative motion was negligible and consequently not corrected.

An uncertainty analysis has been conducted which is based on an approach suggested by Lazar et al. (2010). The analysis takes into account the equipment-related uncertainty, the uncertainty due to the particle lag and the sampling uncertainty. The equipment-related uncertainty includes calibration and timing error. The approach for the calculation of the sampling uncertainty is extracted from Benedict and Gould (1996). The total uncertainty for *FOV1* is largest for the Mach 0.9-case and amounts to ± 3.6 with respect to the incoming flow velocity U_C . For *FOV2*, the uncertainty is in the range of $\leq \pm 3$ to 4%. For the turbulent quantities, only the 95% confidence interval of the sampling uncertainty according to Benedict and Gould (1996) is provided as shading in the corresponding graphs (Figs. 4, 11, 12, 16, 17). The confidence interval for boundary layer thickness in Table 2 has been determined by means of a Monte Carlo simulation imposing the previously determined velocity uncertainty levels.

Further, the results have been checked for peak locking, which in consequence was ruled out, and with respect to the signal-to-noise ratio. The latter has been assessed for the cross-correlation of the interrogation windows and for two-point correlations of the velocity field in the region where turbulence is homogeneous, meaning in the streamwise direction of the boundary layer. To provide quantitative data, the signal-to-noise ratio of the cross-correlation plane is given for a rectangular box in the near-wake flow configuration (*FOV1*) at Mach 0.8. In detail, this rectangular box is situated at $0.1 \leq x/D \leq 1.2$ and $0.22 \leq r/D \leq 0.5$. There, the mean signal-to-noise ratio is ≥ 9 . Data to the particle image size is difficult to provide, since the seeding density is relatively high. Individual particle images are rare, which makes a automated approach for the acquisition of this quantity very challenging. An assessment by eye returns a particle image size of about two to three pixels.

As in the preceding study, one objective of the close-up (*FOV2*) data is the analysis of the incoming boundary layer properties. For that reason, the profile up to 98% of the edge velocity u_e is used for a fitting (see Ref. Berg 1977) to the law of the wake (e.g., White (1991), Schetz and Bowersox (2011)). The law of the wall including the wake (law of the wake) for incompressible turbulent boundary layer flows is given in Eq. 1. Clauser's values (Clauser 1956) are used for κ and B , which are in this case equal to 0.41 and 4.9, respectively. The velocity u and the distance to the wall Δr are normalized to the dimensionless distance to the wall r^+ and the dimensionless velocity u^+ by means of the shear stress velocity u^* and the kinematic viscosity ν as shown in Eq. (2). The boundary layer thickness is given by δ_{99} , and for the description of the wake, a sine ansatz with Coles' wake parameter Π is used (see e.g. Ref. Schetz and Bowersox

2011). Further, boundary layer characterizing parameters are provided for comparisons: Eqs. (3) and (4) describe the displacement thickness δ^* and the momentum thickness θ . The shape factor H_{12} is defined as the ratio between the two, ergo $H_{12} = \delta^* / \theta$.

$$u^+ \approx \frac{1}{\kappa} \ln(r^+) + B + \frac{2\Pi}{\kappa} \sin^2\left(\frac{\pi}{2} \frac{\Delta r}{\delta_{99}}\right), \quad (1)$$

$$u^+ = \frac{u}{u^*}; \quad r^+ = \frac{\Delta r u^*}{\nu}, \quad (2)$$

$$\delta^* = \int_0^{\delta_{99}} \left(1 - \frac{u}{U_C}\right) d\Delta r, \quad (3)$$

$$\theta = \int_0^{\delta_{99}} \left(1 - \frac{u}{U_C}\right) \frac{u}{U_C} d\Delta r. \quad (4)$$

For some selected locations (Sect. 3.3), velocity samples were extracted and analyzed by means of their probability density estimate. The estimate is based on a normal kernel function and is evaluated over a range of 100 equally spaced points of the velocity data.

3 Results

The subsections present results to the incoming boundary layer in Sect. 3.1, to the near-wake flow in Sect. 3.2, and to outstanding points in the flow field in Sect. 3.3.

3.1 Inflow conditions and upstream boundary layer

The boundary layer along the main body is described in the following to provide details about the incoming flow conditions, since the ratio between boundary layer thickness and step height of a backward-facing step is an important similarity parameter (Westphal et al. 1984). Thus, the data are intended for comparisons with similar studies, and as done in the introduction for comparisons with the real flight.

The trend of the mean boundary layer in terms of the inner scaling as found from the least-square fitting to the law of the wake (Eq. 2) is shown in Fig. 3 for Mach 0.6–0.9. The plot additionally shows the trend for a boundary layer on a flat plate, the viscous sublayer and the law of the wall. The trend on a flat plate is given as reference only for the Mach 0.9-configuration, since no substantial deviations to the other Mach numbers were notable. Note that no measurements on the boundary layer were done for Mach 0.5-case, simply due to the time constraints of the measurement campaign.

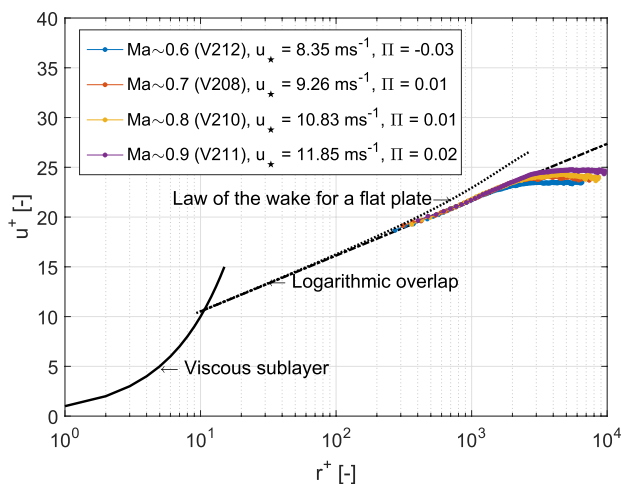


Fig. 3 Boundary layer profiles for the investigated inflow Mach numbers fitted to the law of the wall (with wake). The law of the wake for the flat plate is based on $\Pi = 0.51$, $u^* = 11.8 \text{ ms}^{-1}$ and $\delta_{99} = 3.39 \text{ mm}$

The outcomes seem to be identical to the configuration without jet (Saile et al. 2019): First, the boundary layer follows closely the logarithmic trend of the law of the wall, and second, the boundary layer and the corresponding fitting reveal no wake in the boundary layer profile. For the configuration without jet, this was expected and explained with the favorable pressure gradient in the wind tunnel nozzle (Saile et al. 2019). Here, the exhaust jet acts as an additional driver, since it induces a further reduction of the base pressure causing an increase of the base suction effect (e.g. Schoones and Bannink 1998; Deprés et al. 2004; Wolf 2013). For instance, Deprés et al. (2004) reports of a relatively far-reaching ($x/D < -0.3$), pressure-decreasing upstream influence of the recirculation region on the boundary layer. This ejection influence of the jet is confirmed by the pressure measurements, but not shown in the current frame of the work here.

The low-pressure environment at the base separation and the inherent acceleration of the ambient flow are accompanied with a thinning of the boundary layer thickness in comparison to the configuration without jet (Saile et al. 2019). Boundary layer-related parameters like the boundary layer

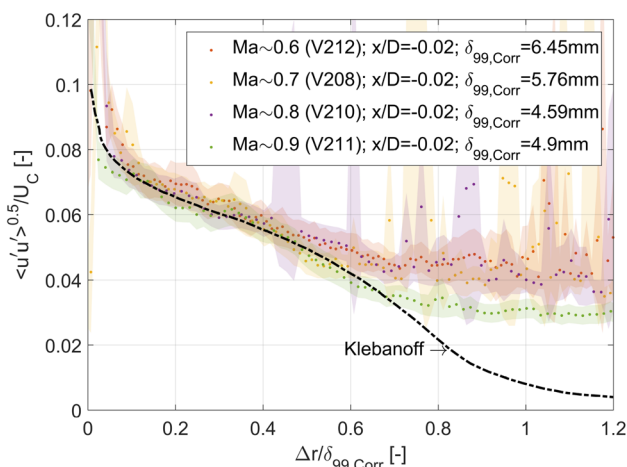


Fig. 4 Turbulence intensity profiles of the boundary layer at $x/D = -0.02$ normalized with boundary layer thickness of the configuration without exhaust jet. In detail: $\delta_{99} = [6.45, 5.76, 4.59, 4.9] \text{ mm}$ for Mach = [0.6, 0.7, 0.8, 0.9]

thickness δ_{99} , displacement thickness δ^* , and the momentum loss thickness θ are presented in Table 2 relatively to the step height h . A boundary layer is considered as thin if the ratio δ_{99}/h takes values below 0.4 (Adams and Johnston 1988). The shape parameter H_{12} is additionally provided. As further parameters of Table 2, the fitting results are captured, namely the Coles' wake parameter Π and the shear stress velocity u^* . The first parameter Π at about zero reflects the weak development of the wake in the boundary layer profile.

The turbulence intensity just upstream from the edge ($x/D = -0.02$) is plotted in Fig. 4 along with the results for a flat plate with no pressure gradient as acquired by Klebanoff (1955). Instead of using the measured boundary layer thickness of the case with jet for the non-dimensionalization, the boundary layer thickness of the case without jet is used (Saile et al. 2019). As a result, the turbulence intensity snuggles up to the results by Klebanoff (1955). Before, for the case of a non-dimensionalization of the boundary layer thickness with jet, the overall turbulence intensity was at a higher level. For instance at $\Delta r/\delta_{99} = 0.5$,

Table 2 Free-stream conditions and parameters with respect to the inflow boundary layer at $x/D = -0.02$ of the FOV2 evaluation

Run ID	VMK			Model		Boundary layer					
	$Ma_C (-)$	$U_C (\text{ms}^{-1})$	$Re_D (-)$	$p_{0,b} (\text{MPa})$	$T_{0,b} (\text{K})$	$\delta_{99}/h (-)$	$\delta^*/h (-)$	$\theta/h (-)$	$H_{12} (-)$	$u^* (\text{ms}^{-1})$	$\Pi (-)$
V212	0.59	195.8	1.0×10^6	3.30	281.8	0.17 ± 0.0086	0.021	0.013	1.64	8.3	-0.03
V208	0.68	222.2	1.2×10^6	3.26	286.4	0.17 ± 0.0083	0.022	0.013	1.67	9.3	0.01
V210	0.79	261.4	1.4×10^6	3.25	284.1	0.16 ± 0.0085	0.017	0.013	1.36	10.8	0.01
V211	0.89	292.7	1.6×10^6	3.26	282.6	0.17 ± 0.0083	0.018	0.013	1.28	11.9	0.02

it was— depending on the Mach number case—20 to 30% higher. It seems like the acceleration has led to a decrease of the boundary layer thickness, but not of incoming turbulence intensity inside of the boundary layer. At a farther radial distance from the wall, the trend deviates from the prediction and converges to the level of the facility's free-stream turbulence intensity.

In summary, the boundary layer exhibits turbulent characteristics, which can be found in the mean flow and as well in turbulent quantities. The form of the wake in the boundary layer profile (Fig. 3) reveals that the flow is accelerated over the edge of the base. The ejection effect due to the jet presumably leads to an increased base suction (see Ref. Schoones and Bannink 1998; Deprés et al. 2004; Wolf 2013), meaning lower base pressure, which in turn decreases the incoming boundary layer thickness.

3.2 Wake flow and Mach number dependency

The preceding study (Saile et al. 2019) evidenced similar flow fields in the wake for a configuration without jet if scaled with the reattachment length. In the following, the near-wake flow with a cold, over-expanded, supersonic jet is evaluated with respect to the similarity characteristics in the mean and turbulent wake flow distribution in Sects. 3.2.1 and 3.2.2, respectively. Further, the overall dependency on the Mach number is assessed.

3.2.1 Mean velocity distribution

The mean flow velocity measured by PIV is shown in Fig. 5 for the investigated Mach numbers. It can be seen that the increase of the Mach number results in an elongation of the recirculation bubble and a downstream shift of the mean reattachment location and vortex center. For Mach numbers ≤ 0.8 , the mean reattachment presumably takes place on the solid nozzle wall. At Mach 0.9, the separated recirculation bubble extends all the way up to the jet where a reattachment on the jet can be found. In comparison to the previous rather incremental change of the reattachment length, one can observe a 'sudden' elongation of the mean recirculation bubble for this Mach 0.9-case.

Both characteristic locations, meaning the mean vortex center x_{vc} and reattachment length L_r , are captured in Table 3. In comparison to the configuration with no exhaust jet (Saile et al. 2019), the reattachment length is smaller. The upstream shift of the reattachment location is attributed to the pressure decrease in the base region due to entrainment induced by the jet. This appears to impose a stronger deflection of the shear layer toward the axis, an observation of which Wolf (2013) has also reported.

As executed for the configuration without jet, the flow field is scaled in the following with the mean reattachment

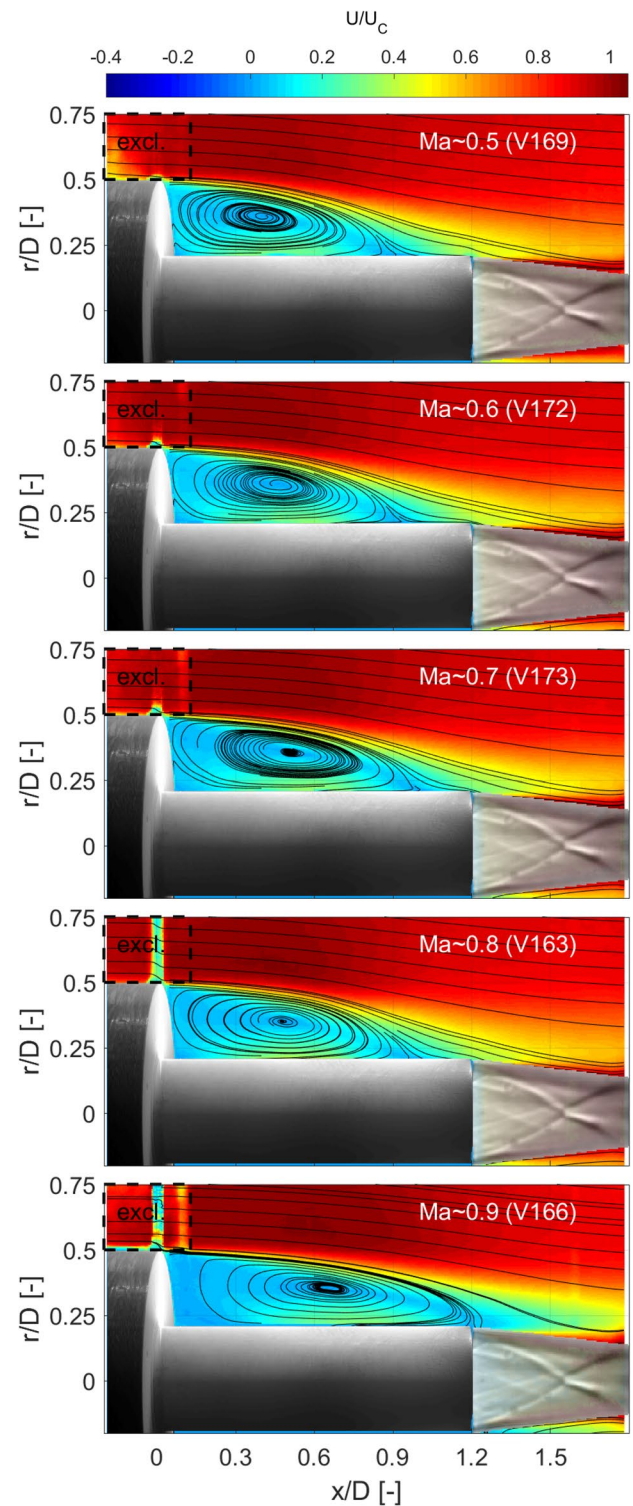


Fig. 5 Contour plots with streamlines of the mean flow field for $Ma \sim 0.5, 0.6, 0.7, 0.8, 0.9$. The region with erroneous data is marked with *excl.* for excluded

Table 3 Location of the vortex center, the reattachment and the ratio between both

Run ID	Mach number Ma_C	Vortex center $[(x, r)/D]_{vc}$	Reattach. length L_r/D	Ratio x_{vc}/L_r
V169	0.49	[0.41, 0.35]	0.87	0.47
V172	0.59	[0.47, 0.36]	0.89	0.53
V173	0.69	[0.51, 0.36]	0.97	0.53
V163	0.79	[0.48, 0.35]	0.94	0.51
V166	0.89	[0.66, 0.36]	1.25*	0.53

A pseudo-reattachment location (marked with *) is given for the configuration with reattachment on the jet (V166). The subscript vc is associated with the vortex center

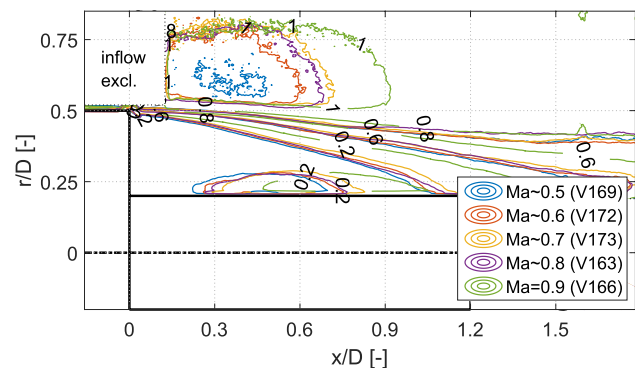


Fig. 6 Iso-contour lines of the normalized mean velocity field scaled with the base diameter

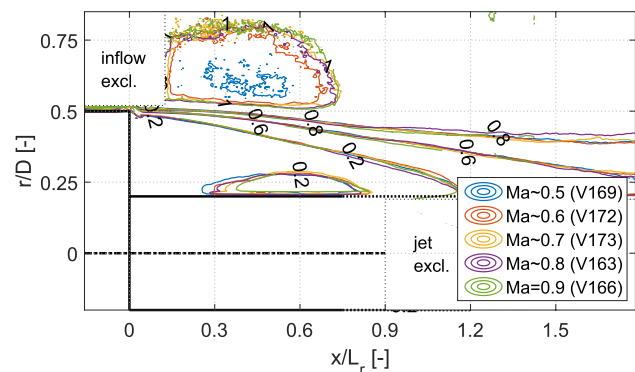


Fig. 7 Iso-contour lines of the normalized mean velocity field scaled with the reattachment length

length. For Mach 0.9, the reattachment takes place on the jet. Thus, the pseudo-reattachment length of 1.25 is determined by means of the ratio x_{vc}/L_r found for the lower Mach number cases, here 0.53, and the mean vortex center location of the recirculation bubble $x_{vc} = 0.66$. Those before and after scaling are shown in Figs. 6 and 7, respectively. The result is slightly more ambiguous, as for the configuration without jet

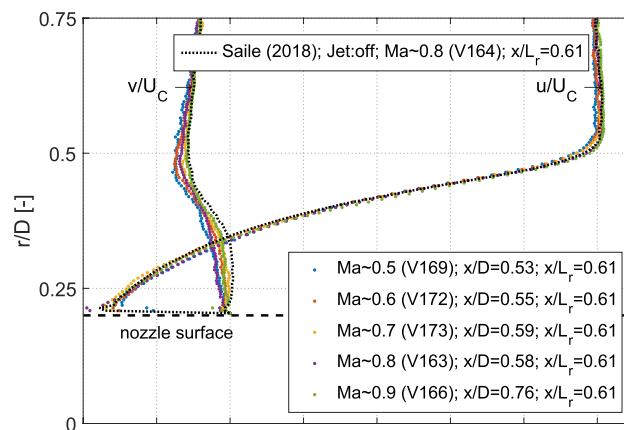


Fig. 8 Normalized mean velocity profiles in the stream-wise and radial direction for the downstream location $x/L_r = 0.61$

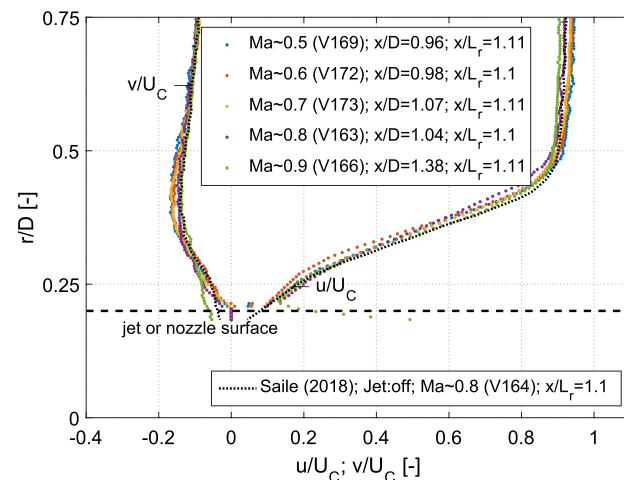


Fig. 9 Normalized mean velocity profiles in the stream-wise and radial direction for the downstream location $x/L_r = 1.1$

since small deviations can be found in the recirculation bubble in the range $x/L_r \sim 0.3$. But generally, the reattachment scaled velocity field (Fig. 7) shows a very good agreement of the iso-contour velocity lines for the various Mach numbers.

Correspondingly, this finding must be supported by the radial profile slices, which are depicted in Figs. 8 and 9 for a location upstream and downstream of the mean reattachment location, more specifically at $x/L_r = 0.61$ and 1.1, respectively. Supplementary, the mean profile of the Mach 0.8-case without jet (extracted from Saile et al. (2019)) is plotted for comparisons. It seems like the reattachment scaled velocity profiles actually share similar trends. A reasonably good agreement of the reattachment scaled velocity profiles can be found for both: between the different Mach numbers (with jet) and between the configuration with and without jet for all extracted slices. Thus, these profiles provide further evidence to a reattachment-scaled similarity of the near-wake

flow. It is even maintained for the reattachment on the jet at Mach 0.9 (Fig. 9). For that case, however, it can be seen that the flow in the mixing layer (to the jet) is getting accelerated, meaning the profiles differ there ($r/D < 0.25$). But outside of the jet, the velocity profiles almost collapse.

An intrinsic result of this similarity is the similarity with respect to evolution of the vorticity in succession from the base separation. This was discussed in Saile et al. (2019) for the case without jet and was also investigated in the frame of the study at hand. In fact, the results revealed that the vorticity thickness equally appears to scale with the reattachment length for all Mach numbers. Thus, it supports the observation of similar flow characteristics. However, to limit the length of the study, it is not shown here.

3.2.2 Velocity fluctuation distribution

The observation of similar flow features is tested in the following for turbulent quantities. Further, an overview of the velocity distribution in dependence of the investigated Mach numbers is provided.

3.2.2.1 Axial turbulence intensity Figure 10 shows the normalized axial turbulence intensity response to increasing Mach numbers. The graphs reveal elevated normal stress levels within the shear layer and the recirculation bubble. For the latter, it can be seen that the excited region travels downstream for larger Mach numbers. In most cases, both excited areas merge downstream from the center for the recirculation bubble.

An anomaly can be found for Mach 0.8. The Mach 0.8-case shows a striking separation between the excited regions with three individual maxima. As the most distinct region the maxima appears in the recirculation bubble marked with P2. Other areas of high turbulent intensity can also be detected in similar form for the other Mach numbers, such as the maximum close to the separation or the maximum in the shear layer. Thus, questions concerning the origin of that high turbulent intensity patch arise. Moreover, this finding challenges the observation regarding the similarity for the turbulent quantities. Note that the P1 marker is discussed later in the frame of outstanding locations in Sect. 3.3.

To analyze further details regarding the anomaly, profile plots of the turbulent intensity are provided in Figs. 11 and 12 for two different locations in the downstream direction. Figure 11 shows this quantity inside the recirculation bubble at the reattachment length scaled location $x/L_r = 0.61$. Except for Mach 0.8, generally the same trend can be observed and the maxima exhibit the same order of magnitude. Thus, for these Mach numbers, the wake flow appears to be independent of the Mach number and independent of the presence of a jet. Outstanding is the trend for Mach 0.8. There, the high turbulence region detected in the

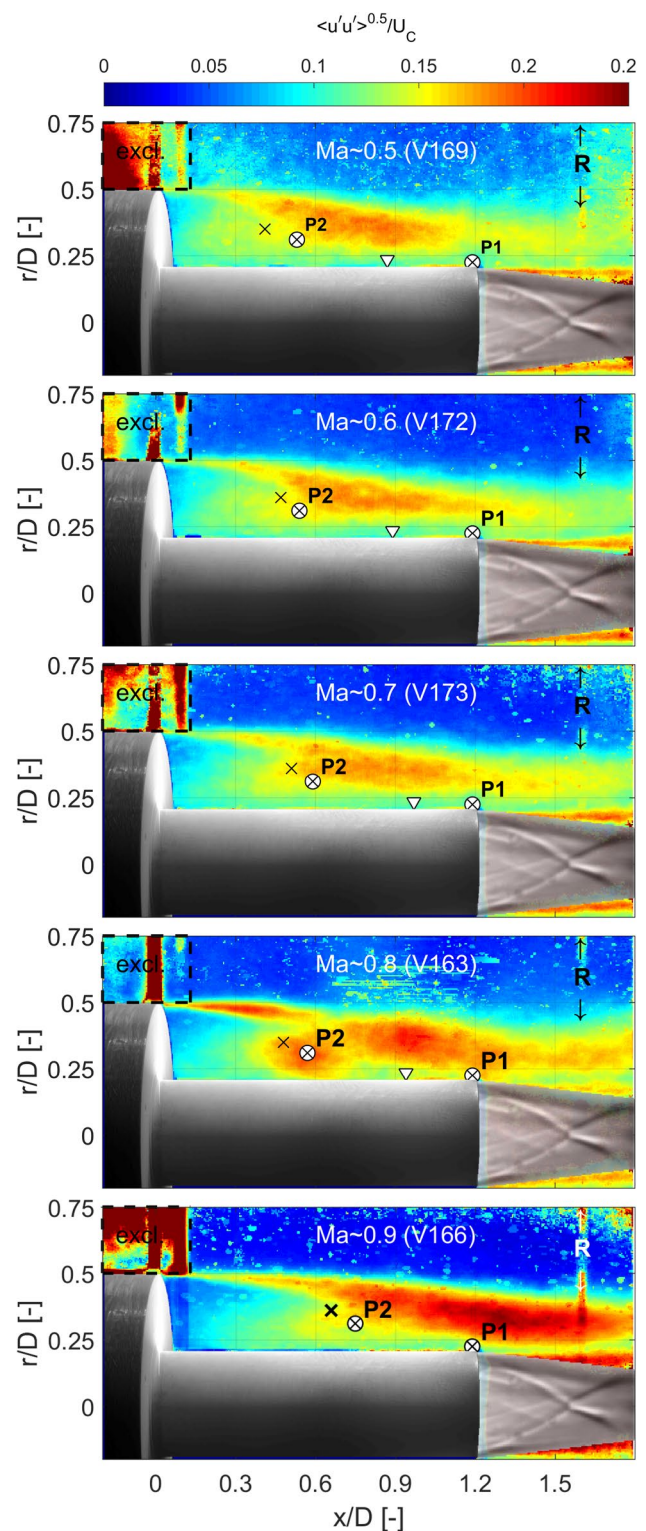


Fig. 10 Contour plots of the normalized axial turbulence intensity field for $Ma \sim 0.5, 0.6, 0.7, 0.8,$ and 0.9 . The center of the main vortex and the reattachment location are plotted as cross \times and as triangle ∇ , respectively. The regions with erroneous data are marked with *excl.* and *R* for excluded and reflections, respectively

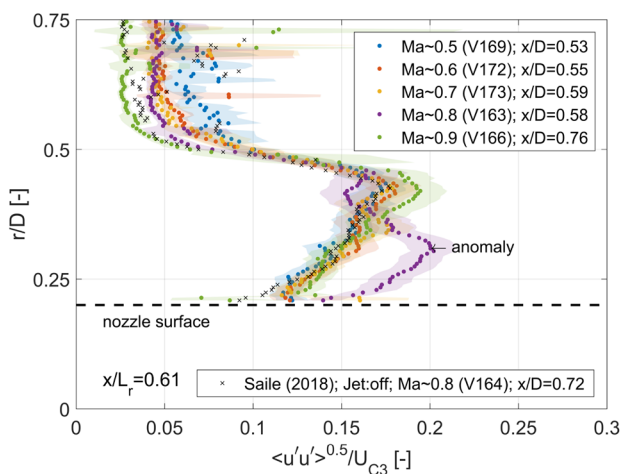


Fig. 11 Normalized axial turbulence intensity profiles for the downstream location $x/L_r = 0.61$. Shading reflects uncertainties as described in Sect. 2

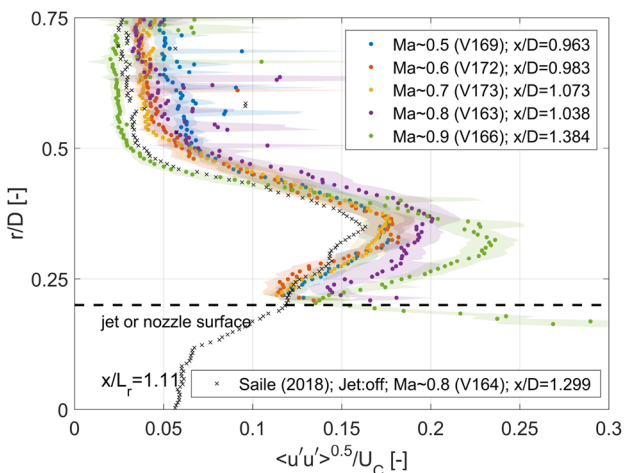


Fig. 12 Normalized axial turbulence intensity profiles for the downstream location $x/L_r = 1.11$. Shading reflects uncertainties as described in Sect. 2

contour plots is clearly captured as an exceptionally excited area in the recirculation bubble.

Farther downstream at $x/L_r = 1.1$, Fig. 12 shows that the profiles for Mach numbers ≤ 0.7 nearly coincide. Thus, this data set provides evidence for the validity regarding the flow similarity as long as the reattachment clearly takes place on the solid nozzle. The deviation for Mach 0.8 obviously still persists and another deviation can be found for Mach 0.9. There, elevated turbulent intensities can be detected in the wake region, which might be introduced by the open interface of the recirculation region to the jet.

Reynolds shear stress The basic observations from above can be repeated and transferred for the description of the

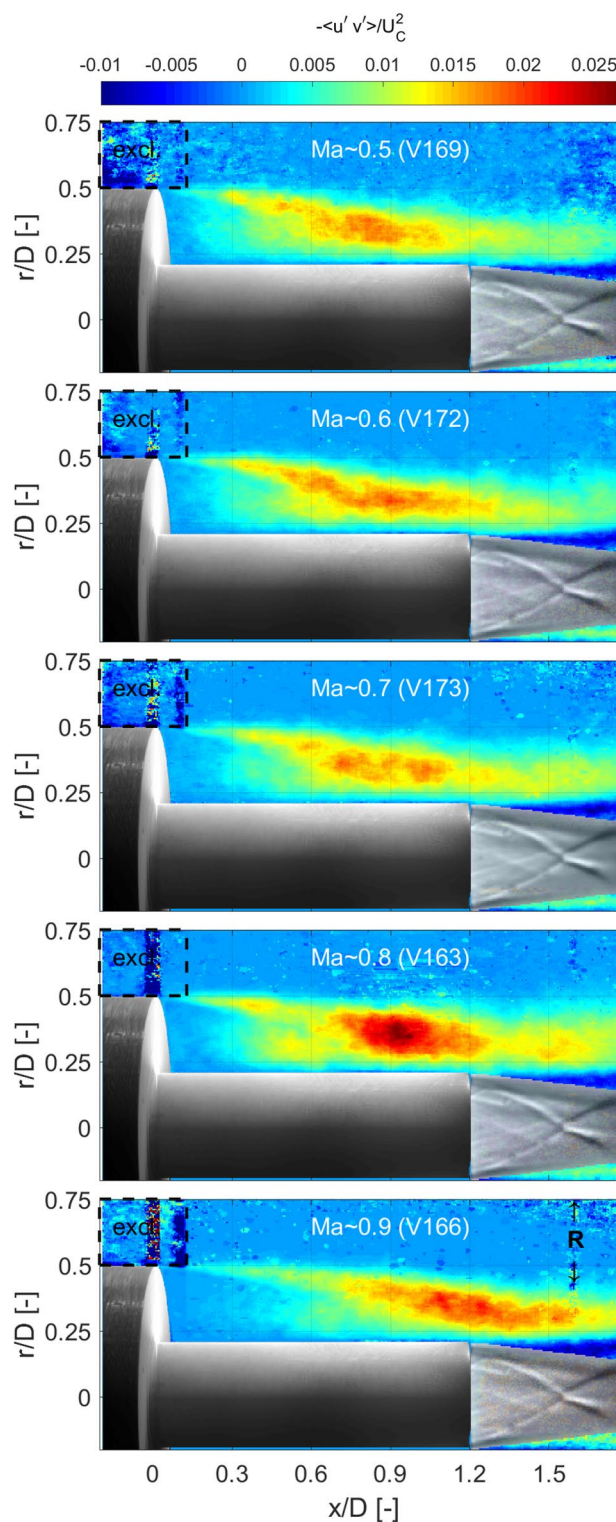


Fig. 13 Contour plots of the normalized Reynolds shear stress field for $Ma \sim 0.5, 0.6, 0.7, 0.8,$ and 0.9 . The regions with erroneous data are marked with *excl.* and *R* for excluded and reflections, respectively

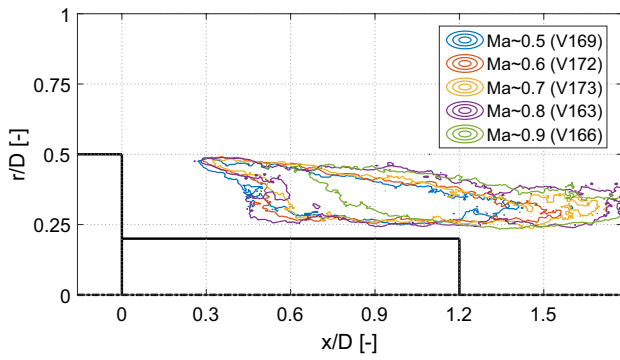


Fig. 14 Iso-contour plot lines of the normalized Reynolds shear stress at $\langle u'v' \rangle = 0.01$ scaled with the base diameter

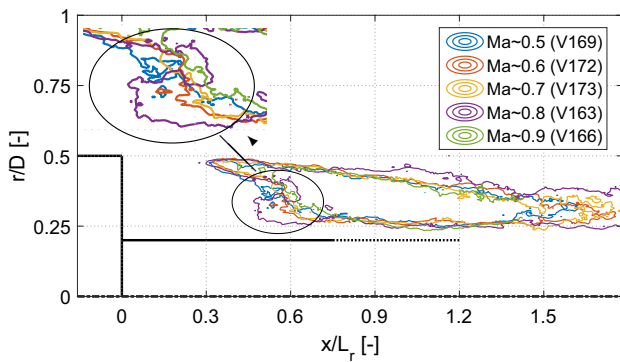


Fig. 15 Iso-contour plot lines of the normalized Reynolds shear stress at $\langle u'v' \rangle = 0.01$ scaled with the reattachment length

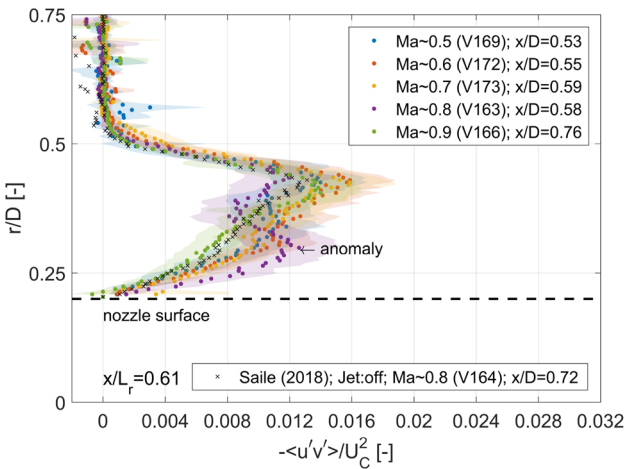


Fig. 16 Normalized Reynolds shear stress profiles for the downstream location $x/L_r = 0.61$. Shading reflects uncertainties as described in Sect. 2

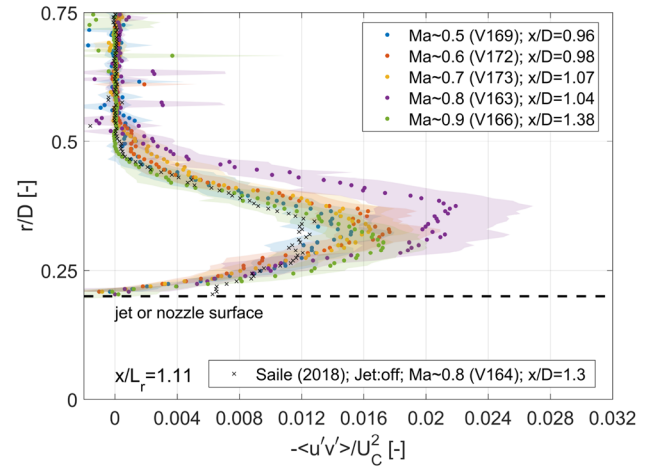


Fig. 17 Normalized Reynolds shear stress profiles for the downstream location $x/L_r = 1.11$. Shading reflects uncertainties as described in Sect. 2

normalized Reynolds shear stress distribution, which is shown in Fig. 13. The two excited areas as imprints of the shear layer excitation and the excitation in the recirculation bubble can also be found here. Moreover, the maximum Reynolds shear level seems to be at about a constant level up to Mach 0.7 and increases substantially to the largest measured value for that Mach 0.8 before easing off for 0.9.

As above, the reattachment length scaling approach is assessed by means of an iso-contour plot. Both scaling versions are supplied: the scaling with the base diameter is shown in Fig. 14; the one with the reattachment length scaling is depicted in Fig. 15. On the one hand, it can be seen that a relatively good agreement is achieved for the reattachment length scaling; on the other hand, one can also observe that the iso-lines do not concur for the anomaly at Mach 0.8.

Quantitative Reynolds shear stress profiles for all Mach numbers are provided for a location inside the recirculation bubble ($x/L_r = 0.61$) and downstream from the reattachment ($x/L_r = 1.1$) in Figs. 16 and 17, respectively. Again, the results for the configuration without jet are given for comparisons. Figure 16 captures the area where the merger between the intensified turbulent area in the recirculation bubble and the shear layer takes place. Except for the Mach 0.8, the reattachment length-scaled trend seems to be comparable. For Mach 0.8 however, an exceptional amplification is again detectable in the recirculation bubble.

This tendency is maintained farther downstream at $x/L_r = 1.1$ where the Mach 0.8-case still returns notably larger Reynolds shear stress levels. The peak level is about 25% higher than the next closest profile maximum of any other Mach number. As another distinguishing feature to the trends of the other Mach numbers, one can see that the radial extent of the increased stress is relatively seen larger, which

indicates a wider influential range of the shear layer. In contrast to this anomaly, the Reynolds shear stress levels of the lower Mach numbers are smaller and the trends among them are similar. Also, the Reynolds shear stress level for Mach 0.9 is surprisingly similar to the lower Mach number cases despite exhibiting clear differences in turbulent intensity as shown above in Fig. 12. Thus, it seems like the Mach 0.8-case poses a special case where velocity fluctuations are especially excited. For now, the PIV measurements indicate that this excitation effect might be interrelated with the shear layer reattachment location or more specifically with the shear layer reattachment process.

Focusing on the radial profiles again, the presence of the jet seems to moderately increase the turbulence in the wake without presumably altering the overall dynamics. With the exception of the anomaly, the curve in Fig. 16 of the case without jet features comparable trends as the counterpart with jet. The excitation level (at $x/L_r = 0.61$) appears to be about 15% to 20% lower. Downstream from the reattachment location $x/L_r = 1.1$, the difference is in the range of 25%.

In summary, the Reynolds stress level of the cases that feature a predominantly closed recirculation region differs significantly from the configurations that have an open recirculation region or one that clearly interacts with the jet. The Mach 0.8-case is outstanding since its Reynolds stress level is clearly larger. It features an excited region below the center of the mean vortex center and close to the wall (see, e.g., profile at $x/L_r = 0.61$, Fig. 16), which is not present to such a degree for the other Mach numbers. Further, the highest level of magnitude can usually be found where the shear layer flapping is assumed in the vicinity of the mean flow reattachment location. Then, the Mach 0.9-case shows again more similarities to the low Mach number cases ($Ma \sim 0.5$ to 0.7). Generally, the near-wake region downstream from the reattachment is more energetic with exhaust jet.

3.3 Probability density estimate and instantaneous velocity distribution

As a common denominator of the previously described results, one can state that a distinct effect takes control at about Mach 0.8, which forces a different response upon the mean and unsteady flow dynamics in the flow field. For this reason, the probability density estimates function (PDF) of the velocity samples of two ‘outstanding’ points are presented in the following. Further, instantaneous velocity fields are given to provide evidence for the origin of characteristic traits. Please be aware that the instantaneous velocity fields cannot be used for the generalization of a finding, but they serve the purpose of giving possible explanations for the PDF and high Reynolds stress locations.

The first point denoted as P1 is located just upstream of the nozzle exit. This point is fixed for all Mach numbers at

$[x, r]/D = [1.19, 0.22]$, which is in contrast with the second point P2. That point focuses on the maximum of the distinct and isolated increased turbulence intensity area inside the recirculation bubble found for Mach 0.8. The P2 points for the other Mach number cases are scaled appropriately with their corresponding reattachment length.

3.3.1 Location upstream from the tip of the nozzle

The point P1 just upstream of the nozzle exit was selected to address the reattachment process. As indicated in Fig. 18 by the exclusively downstream pointing velocity components u/U_C of the PDF distribution for $Ma \leq 0.8$, reattachment seems to take place for all occasions on the solid nozzle wall. Further, the Mach 0.7-case is remarkable since the axial distribution shifts to lower velocities. Then for 0.8, the range of probable velocities has suddenly widened, meaning smaller axial velocity components become more frequent, while relatively high velocity are simultaneously more common. At Mach 0.8 for instance, about 17% of the samples exhibit an axial velocity u/U_C larger than 0.5, while this barely occurs for any other Mach number. The larger spread of the probability range evidences the increased turbulent intensity as observed in Fig. 10. Finally, at Mach 0.9, the largest share of the flow at point P1 points upstream (71.4%), which suggests an alternating (hybrid) shear layer reattachment on the solid nozzle wall and jet, or in other words, a temporally open interface between the recirculation bubble and the jet. This is where the jet can directly interact with the recirculation region.

Of interest now is what the instantaneous velocity field looks like in the ‘off-average’ and/or critical scenarios (such

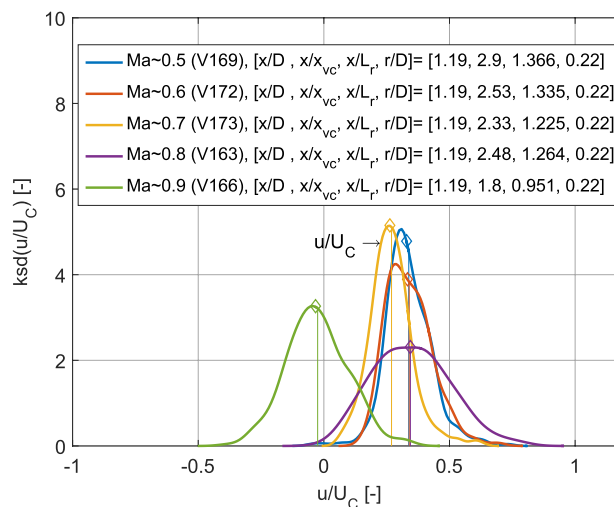


Fig. 18 Probability density estimate of the axial normalized velocity sampled upstream from the nozzle exit at point P1. Diamond \diamond markers denote the normalized mean axial velocity; the thin continuous line the median velocity

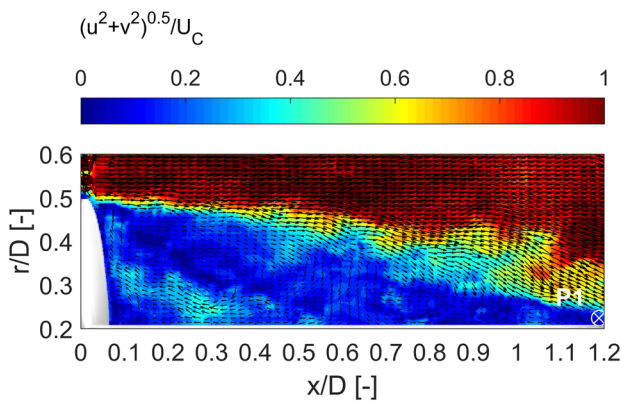


Fig. 19 Instantaneous velocity distribution for the Mach 0.8-case (V163) to exemplarily visualize a low axial velocity situation ($u/U_C = 0.12$) at point P1 just upstream from the nozzle exit. Every fourth and second vector is shown in x - and r -direction, respectively

as for Mach 0.8) when the stream-wise velocity is either relatively small or large with respect to the probability density function just upstream from the nozzle exit at P1. Figure 19 shows exemplarily a Mach 0.8-case on the low speed side of the velocity range. For that case, the velocity at point P1 exhibits just 12% of the mean incoming velocity U_C . The reason for the relatively low velocity seems to be that the shear layer overshoots the nozzle and reattachment takes place on the jet. The vortical base flow region is stretched to the size where it can interact with the jet, or, in other terms, is open. This is in contrast to the cases where the shear layer reattaches on the nozzle wall, which are more frequent and can be found, e.g., in Fig. 21. Thus, as a result, it can be stated that an ‘open’ recirculation bubble starts to develop for the Mach 0.8-case, which in turn seems to be interrelated with the observed anomaly.

3.3.2 Location inside the recirculation bubble

The probability density estimate in the high turbulence intensity region (P2) is depicted in Fig. 20. Except for the Mach 0.8-case, the shape of the axial PDFs look relatively similar: the normalized mean and median can be found in about similar velocity ranges and the curves collapse with a reasonable agreement. The exceptional Mach 0.8-case features, as expected from the turbulence intensity plots (Fig. 10), a larger spread of axial velocities. This extension of the spread can be found for both flow directions: upstream and downstream.

The instantaneous velocity fields shown in Fig. 21 help to shed light on the question about the magnitude of the turbulence intensity at that position P2. The instantaneous velocity distribution suggests that the large spread is caused by a ‘dancing’ large vortical structure. At one point in time, the vortex center is located above (at a farther radial distance)

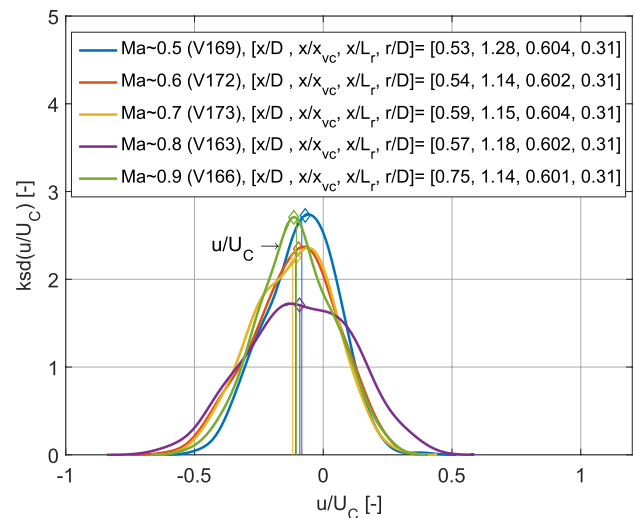


Fig. 20 Probability density estimate of the axial normalized velocity sampled at the turbulence intensity maximum (for Mach 0.8) in the upstream region (P2). For further denotations, see Fig. 18

the spatially fixed point P2, while at another point in time, it is below. Hence, relatively large downstream and upstream velocity contributions are added to the velocity range. This wide spread then explains for the maximum turbulent intensity at that location. The top graph shown here presents a case where the axial upstream velocity takes on 54% of the

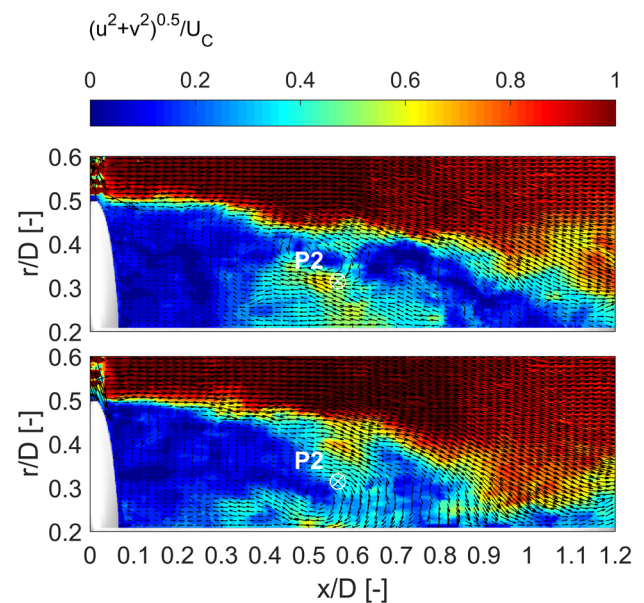


Fig. 21 Instantaneous velocity distribution for the Mach 0.8-case (V163) to exemplarily visualize a large axial upstream (top: $u/U_C = -0.54$) and downstream (bottom: $u/U_C = 0.31$) velocity situation at point P2 at the local maximum turbulence intensity patch. Every fourth and second vector is shown in the x - and r -direction, respectively

incoming flow, while for the bottom graph, the downstream velocity accounts for 34%.

4 Discussion

In the following, the observations from before are collected and discussed with respect to the reattachment length scaling and the anomaly. The first topic is addressed in Sect. 4.1 and the second in Sect. 4.2.

4.1 Considerations to the reattachment length scaling

Evidence for a similarity regarding the nature of the near-wake flow was given in the preceding study for the same configuration, but without jet (Saile et al. 2019). Now, similar characteristics appear to be present for the configuration with supersonic jet. The preceding findings are backed by the good agreement with the numerical and experimental results by Weiss and Deck (2013), which are consequently also seen as an anchor point for the current results. Major deviations are found for the ‘anomaly’ (Sect. 4.2).

In literature, reattachment length-based scaling for recirculation bubbles was introduced for the normalization in a spatial and temporal sense by Roshko and Lau (1965) and Mabey (1972), respectively. For backward-facing step configurations with thin boundary layers, Adams and Johnston (1988) found the pressure rise curve to be similar for various Reynolds numbers. Further, for the subsonic range between $0.11 < Ma < 0.94$, Merz et al. (1978) found similarity of the centerline velocity distribution in the near-wake for a blunt axisymmetric body. More recently, Nadge and Govardhan (2014) investigated the flow over a backward-facing step by means of PIV measurements. For Reynolds numbers $Re_h > 36,000$, the flow showed to be about independent of Reynolds number: The normalized mean velocity fields and the normalized turbulent stresses showed to be similar.

For the current space launcher configuration with jet, similar characteristics are found among the various Mach numbers for the lower investigated Mach (Mach 0.5–0.7) and corresponding Reynolds numbers except for the cases where the reattaching shear layer interacts with the jet (Mach ≥ 0.8). The turbulent quantities of the Mach 0.8-case deviate notably in comparison to the low Mach number cases. The Mach 0.9-case though surprisingly exhibits elements that compare well with the former. Thus, the discussion in the following paragraph only refers to the lower Mach numbers. The Mach 0.9-case is discussed in the subsequent paragraph.

The previously mentioned similarity observations concern the mean velocity and Reynolds stress distribution. For these quantities, it is shown in Figs. 7 and 15 that the applied scaling appears to be appropriate. Inside the mean

separation region, the contour lines of the velocity and Reynolds stress align. More details to this presumable similarity are evidenced in the profile plots for the mean flow (Fig. 8), the turbulence intensity (Fig. 11) and Reynolds shear stress (Fig. 16). Further, these observations seem to be inherent in the curves of the probability density estimate functions (PDFs) of the local maximum turbulence intensity at point P2 (Fig. 20): The first and second moments, meaning the average and standard deviation, coincide to a reasonable degree.

For the Mach 0.9-case, the scaling is done with a pseudo-reattachment length since the shear layer does not reattach completely on the solid nozzle wall for these conditions. Nevertheless, the Mach 0.9-case also seems to share some of the similar traits: the mean velocity profiles (Fig. 8, 9) coincide; at the upstream location ($x/L_r = 0.61$), the turbulence intensity levels are comparable (Fig. 11); the PDFs at the point of maximum turbulence in the wake vortex system P2 (Fig. 20) are reasonably similar.

Further, in the vicinity and downstream from the mean reattachment location ($x/L_r \geq 1.0$), the flow appears to be notably influenced by the jet. The data indicate that the jet adds 20–30% to the Reynolds shear stress levels farther downstream in comparison to the low Mach number cases. This is presumably induced by the flow acceleration due to the ejector effect of the jet.

Overall, one might conclude that the near-wake flow features similar trends for the mean flow if the flow reattaches predominantly on a solid wall. A hybrid reattachment alters the turbulent properties mostly in the vicinity and downstream from the reattachment location by increasing the axial velocity fluctuations.

4.2 Considerations to the anomaly at Mach 0.8

The anomaly is outstandingly notable in the turbulent quantities. An exceptionally excited area can be found in the recirculation bubble in the vicinity of maximum upstream velocity location at about $x/L_r \sim 0.6$ (Figs. 11, 16). The instantaneous velocity fields (Fig. 21) suggest that this augmentation is due to the unsteady occurrence of a large-scale, mass-engulfing, and clockwise-rotating vortex. In particular, the vortex center is not stationary locked. Instead, it can be found at various axial and radial positions, which explains the substantial range of probable velocities at that location. In this context, the image of a ‘dancing’ vortex center was used above. Moreover, as part of the large-scale vortex, strong upstream directed jets develop along the solid nozzle wall occasionally reaching a maximum velocity of up to 80% of the incoming flow. This is about 10% higher than for the other Mach numbers.

Thus, the effect causing the excited area appears to be clarified. The question regarding the driver remains open.

Indications for an answer are provided by the nature of the reattachment process. For Mach 0.7 and smaller, the shear layer reattaches predominantly on the solid nozzle wall. An interaction with the jet can clearly be found for Mach 0.9 (Fig. 18). Correspondingly, the reattachment length experiences a downstream shift with increasing Mach number except for Mach 0.8 where an upstream shift is notable (Table 3, Fig. 5). Mach 0.8 is the case for which the recirculation bubble starts to interact with the jet if the Mach number is continuously increased. A similar observation was made for the configuration with dummy nozzle (Saile et al. 2019) where the shear layer reattachment alternates between a solid reattachment and an overshoot. In summary, the abnormal excitation correlates with the hybrid reattachment of the shear layer.

Not elaborated in the context here, but mentioned to provide an indication for a possible explanation of the anomaly: further evaluations of the current data set by means of a *proper orthogonal decomposition* and the analysis of the base pressure suggest another influence which might contribute to the amplification of the turbulence in the recirculation bubble. The results indicate a coupling between near-wake dynamics and the aeroacoustics of the jet (*screeching*). It appears that this coupling is interrelated with a vortex shedding mechanism from the tail of the nozzle such as observed by Statnikov et al. (2017). Moreover, vortex shedding is essentially an entrainment mechanism which might be connected with the mass-engulfing, large-scale, clockwise rotating vortex in the recirculation bubble. This would constitute a cyclical exchange process. It is planned to address further details in separate studies.

5 Conclusion and outlook

The objective of the current study was to contribute data for a better understanding of the buffet/buffeting effect as it occurs in the base region of space launcher configurations such as Ariane 5 in the subsonic flow regime. Moreover, a confirmation of the previous evidence for a similar velocity and Reynolds stress distribution was addressed now for the case with a cold, supersonic, over-expanded exhaust jet. The objectives were assessed by means of experiments in the VMK wind tunnel facility applying PIV measurements over a broad Mach number range from 0.5 to 0.9. Additionally, data of the inflow boundary layer are provided.

For the wake flow, similar flow characteristics can be found for the mean flow for all Mach numbers. The turbulent quantities agree reasonably well upstream from the reattachment. In the vicinity and downstream from the reattachment location, it can be stated that the presence of the jet increases the Reynolds stresses—depending on the Mach number—by 20–100%.

Further, a frequently occurring, large-scale and clockwise-rotating vortex is found in the separated vortex region, which is held responsible for mass engulfment and inter-related upstream directed jets along the nozzle wall. The unsteadiness or ‘dancing’ of the vortex center is seen as reason for the large velocity variation in that region, ergo for the high level of turbulence intensity. Moreover, it is hypothesized that this engulfment cyclically interacts with an entrainment process driven by a vortex shedding mechanism from the recirculation bubble. The other elevated Reynolds stresses area is attributed to the unsteady flapping motion of the shear layer.

Mach 0.8 is found as the limiting case where the shear layer starts interacting with the region at the nozzle end. Due to exceptionally high turbulence level in the recirculation bubble, this limiting case is referred to as ‘anomaly’. It is observed that the upstream directed jets cover an especially wide range of velocities, meaning that the turbulence intensity is pronounced along the nozzle wall where the large, clockwise-rotating vortex is present.

As stated in the introduction, the overarching idea of the current experiments is to provide data related to base flow effects of space launchers. The data can be used for comparisons with numerical tools or as a contribution for the development of design guidelines for launchers. The current experiments show interesting effects with respect of the limiting case when the shear layer just starts to interact with the jet. This is the point where substantial differences regarding the base flow dynamics can be measured. Note that the most critical situation during the ascent of Ariane 5 in terms of oscillations and side loads also occurs at Mach 0.8 (David and Radulovic 2005).

In a next step, experiments where the base geometry was systematically changed will be analyzed for the limiting Mach 0.8-case. As geometrical variation, the nozzle length was shortened. Further, it is planned to publish the analysis of the current data set by means of mode decomposition methods to shed light on the governing motions in the base region, and complementarily, the evaluation of the base pressure data for the discussion of its spectral content.

Acknowledgements Financial support has been provided by the German Research Foundation (Deutsche Forschungsgemeinschaft—DFG) in the framework of the Sonderforschungsbereich Transregio 40. Further, the authors thank the colleagues and the staff for their support!

Open Access This article is distributed under the terms of the Creative Commons Attribution 4.0 International License (<http://creativecommons.org/licenses/by/4.0/>), which permits unrestricted use, distribution, and reproduction in any medium, provided you give appropriate credit to the original author(s) and the source, provide a link to the Creative Commons license, and indicate if changes were made.

References

- Adams EW, Johnston JP (1988) Effects of the separating shear layer on the reattachment flow structure; Part 1: pressure and turbulence quantities. *Exp Fluids* 6(6):400–408
- Benedict L, Gould R (1996) Towards better uncertainty estimates for turbulence statistics. *Exp Fluids* 22(2):129–136
- Berg DE (1977) Surface roughness effects on the hypersonic turbulent boundary layer. PhD thesis, California Institute of Technology
- Clauser FH (1956) The turbulent boundary layer. *Adv Appl Mech* 4:1–51
- David S, Radulovic S (2005) Prediction of buffet loads on the Ariane 5 afterbody. In: 6th symposium on launcher technologies, Munich, Germany, 8–11 November 2005
- Deck S, Thorigny P (2007) Unsteadiness of an axisymmetric separating–reattaching flow: numerical investigation. *Phys Fluids* 19(6):065,103
- Deprés D, Reijasse P, Dussauge J (2004) Analysis of unsteadiness in afterbody transonic flows. *AIAA J* 42(12):2541–2550
- Devenport William J, Schetz, Joseph A (Java, Version 2.1) Boundary Layer Applet. <http://www.engapplets.vt.edu/fluids/bls2/>
- Fuchs H, Mercker E, Michel U (1979) Large-scale coherent structures in the wake of axisymmetric bodies. *J Fluid Mech* 93(01):185–207
- Goethert B (1961) Transonic wind tunnel testing. Tech. rep., Advisory Group for Aeronautical Research and Development, North Atlantic Treaty Organization
- Hannemann K, Lüdeke H, Pallegoix JF, Ollivier A, Lambaré H, Maseand J, Geurts E, Frey M, Deck S, Schrijer F, et al (2011) Launch vehicle base buffeting-recent experimental and numerical investigations. In: 7th European symposium on aerothermodynamics, vol 692, p 102
- Klebanoff P (1955) Characteristics of turbulence in boundary layer with zero pressure gradient. National Advisory Committee for Aeronautics, Report 1247, National Bureau of Standards
- Lazar E, DeBlauw B, Glumac N, Dutton C, Elliott G (2010) A practical approach to PIV uncertainty analysis. In: 27th AIAA aerodynamic measurement technology and ground testing conference, p 4355
- Lüdeke H, Mulot JD, Hannemann K (2015) Launch vehicle base flow analysis using improved delayed detached-eddy simulation. *AIAA J* 53(9):2454–2471
- Mabey DG (1972) Analysis and correlation of data on pressure fluctuations in separated flow. *J Aircr* 9(9):642–645
- Merz R, Page R, CEG P (1978) Subsonic axisymmetric near-wake studies. *AIAA J* 16(7)
- Nadge PM, Govardhan R (2014) High Reynolds number flow over a backward-facing step: structure of the mean separation bubble. *Exp Fluids* 55(1):1657
- Pain R, Weiss PÉ, Deck S (2014) Zonal detached eddy simulation of the flow around a simplified launcher afterbody. *AIAA J*
- Raffel M, Willert CE, Kompenhans J et al (2007) Particle image velocimetry: a practical guide. Springer, Berlin
- Roshko A, Lau JC (1965) Some observations on transition and reattachment of a free shear layer in incompressible flow. In: Charwat AF (ed) Proceedings of the 1965 heat transfer and fluid mechanics institute. Stanford University Press, Stanford, pp 157–167
- Saile D, Kühl V, Gülhan A (2019) On the subsonic near-wake of a space launcher configuration without jet. *Exp Fluids* 60(4):50. <https://doi.org/10.1007/s00348-019-2690-9>
- Saile D, Kirchheck D, Gülhan A, Banuti D (2015) Design of a hot plume interaction facility at DLR Cologne. In: Proceedings of the 8th European symposium on aerothermodynamics for space vehicles
- Scharnowski S (2013) Investigation of turbulent shear flows with high resolution PIV methods. PhD thesis, Universität der Bundeswehr München, Fakultät für Luft- und Raumfahrttechnik
- Scharnowski S, Bolgar I, Kähler C (2016) Interaction of a generic space launcher wake with a jet plume in sub-, trans- and supersonic conditions. International workshop on non-intrusive optical flow diagnostics
- Scharnowski S, Statnikov V, Meinke M, Schröder W, Kähler CJ (2015) Combined experimental and numerical investigation of a transonic space launcher wake. In: Progress in flight physics. EDP Sciences, vol 7, pp 311–328
- Schetz J, Bowersox R (2011) Boundary layer analysis. AIAA Education Series, American Institute of Aeronautics and Astronautics. <https://books.google.de/books?id=GhkqYAAACAAJ>
- Schoones M, Bannink W (1998) Base flow and exhaust plume interaction. Part 1: Experimental study. Series 01: Aerodynamics 15
- Schrijer F, Sciacchitano A, Scarano F (2014) Spatio-temporal and modal analysis of unsteady fluctuations in a high-subsonic base flow. *Phys Fluids* 26(8):086,101
- Schrijer F, Sciacchitano A, Scarrano F, Hannemann K, Pallegoix JF, Maseand J, Schwane R (2011) Experimental investigation of base flow buffeting on the Ariane 5 launcher using high speed PIV. In: 7th European symposium on aerothermodynamics, vol 692, p 103
- Schwane R (2015) Numerical Prediction and experimental validation of unsteady loads on Ariane 5 and Vega. *J Spacecr Rock*
- Statnikov V, Bolgar I, Scharnowski S, Meinke M, Kähler C, Schröder W (2016) Analysis of characteristic wake flow modes on a generic transonic backward-facing step configuration. *Eur J Mech B/Fluids* 59:124–134
- Statnikov V, Meinke M, Schröder W (2017) Reduced-order analysis of buffet flow of space launchers. *J Fluid Mech* 815:1–25. <https://doi.org/10.1017/jfm.2017.46>
- van Gent P, Michaelis D, Van Oudheusden B, Weiss PÉ, de Kat R, Laskari A, Jeon YJ, David L, Schanz D, Huhn F et al (2017a) Comparative assessment of pressure field reconstructions from particle image velocimetry measurements and lagrangian particle tracking. *Exp Fluids* 58(4):33
- van Gent P, Payanda Q, Brust S, van Oudheusden B, Schrijer F (2017b) Experimental study of the effects of exhaust plume and nozzle length on transonic and supersonic axisymmetric base flows. In: 7th European conference for aeronautics and space sciences
- Weiss PÉ, Deck S (2013) Numerical investigation of the robustness of an axisymmetric separating/reattaching flow to an external perturbation using ZDES. *Flow Turbul Combust* 91(3):697–715
- Weiss PÉ, Deck S (2018) On the coupling of a zonal body-fitted/immersed boundary method with zdes: application to the interactions on a realistic space launcher afterbody flow. *Comput Fluids* 176:338–352
- Weiss PÉ, Deck S, Robinet JC, Sagaut P (2009) On the dynamics of axisymmetric turbulent separating/reattaching flows. *Phys Fluids* 21(7):075,103
- Westphal RV, Johnston J, Eaton J (1984) Experimental study of flow reattachment in a single-sided sudden expansion. NASA Contractor Report 3765
- White F (1991) Viscous fluid flow. McGraw-Hill series in mechanical engineering. McGraw-Hill. <https://books.google.de/books?id=G6leAQAIAAJ>
- Wolf CC (2013) The subsonic near-wake of bluff bodies. PhD thesis, Rheinisch-Westfälische Technische Hochschule Aachen, Fakultät für Maschinenwesen
- Wong H, Meijer J, Schwane R (2007) Experimental and theoretical investigation of base-flow buffeting on Ariane5 launch vehicles. *J Propul Power* 23(1):116–122

Publisher's Note Springer Nature remains neutral with regard to jurisdictional claims in published maps and institutional affiliations.